Journal of Materials Chemistry A

PAPER

View Article Online
View Journal | View Issue

Cite this: J. Mater. Chem. A, 2014, 2, 1375

Tetrahexahedral Pt–Pd alloy nanocatalysts with high-index facets: an atomistic perspective on thermodynamic and shape stabilities

Yu-Hua Wen,*[a] Rao Huang,[a] Xiang-Ming Zeng,[a] Gui-Fang Shao[b] and Shi-Gang Sun[c]

Received 11th October 2013
Accepted 12th November 2013

DOI: 10.1039/c3ta14085g

www.rsc.org/MaterialsA

Metallic nanoparticles with high-index facets exhibit exceptional electrocatalytic activity owing to the high density of low coordination sites at the surface, thus they have attracted intense interest over the past few years. Alloying could further improve their catalytic activity by the synergy effects of high-index facets and electronic structures of components. Using atomistic simulations, we have investigated thermodynamic and shape stabilities of tetrahexahedral Pt–Pd alloy nanoparticles respectively bound by {210} and {310} facets. Energy minimization through Monte Carlo simulations has indicated that the outermost layer is predominated by Pd atoms while Pt atoms preferentially occupy the sub-outermost layer of nanoparticles. Molecular dynamics simulations of the heating process have shown that the {210} faceted nanoparticles possess better thermodynamic and shape stabilities than the {310} faceted ones. The coordination numbers of surface atoms were used to explore the potential origin of the different stabilities. Furthermore, a high Pt ratio will help enhance their stabilities. For both faceted nanoparticles, the melting has homogeneously developed from the surface into the core, and the tetrahexahedra have finally evolved into sphere-like shape prior to the overall melting. These results are helpful for understanding the composition and thermodynamic properties of high-index faceted nanoparticles, and are also of practical importance to the development of alloy nanocatalysts.

1. Introduction

Metallic particle catalysts are of growing importance for modern society because of their extensive applications in the chemical industry, the petrochemical industry, environmental protection, and new-energy resources such as fuel cells and lithium ion batteries.[1,2] In the past decades, the rapid development of nanotechnology has made it possible to sufficiently control the particle's size, shape, composition, and morphology at the nanometer level.[3] With particle sizes decreasing to the nanoscale, the particles are formed by a reduced number of atoms and the majority of them are located at the surface, resulting in the remarkably increasing surface-to-volume ratio and more pronounced size effects. These nano-sized particles may exhibit exceptional physical and chemical properties different from those of their bulk counterparts.[4,5]

As is well-known, the catalytic reactions preferentially take place on surfaces, and the catalytic performance of nanoparticles (NPs) highly depends on the structures of facets enclosing the particles.[6] Therefore, understanding the surface structures such as terraces, steps, kinks, adatoms and vacancies, and their effects on catalytic and other chemical properties is crucial for developing metallic NPs of high activity. Because the particle shape is dependent on the crystallographic planes that terminate the particle surface, the shape-controlled synthesis of NPs becomes a promising direction for precisely tuning the activity and selectivity of NP catalysts.[7] After the pioneering work of El-Sayed and co-workers for the synthesis of cubic and tetrahedral Pt NPs,[8] many efforts have been devoted to prepare Pt NPs with different shapes by changing Pt precursors, reducing reagents, stabilizing reagents, and solvents. However, experimentally synthesized Pt NPs are primarily enclosed by low-index facets of {100} and {111}, and few Pt ones with high-index facets are produced by conventional wet chemistry routes.[9–12] Fundamental studies on surface sciences have revealed that Pt high-index planes with open surface structure exhibit much higher reactivity and selectivity than those of low-index planes such as {111} or {100} ones because high-index planes have a large density of low-coordinated atoms situated on steps, ledges, and kinks.[13] However, in solution chemistry, high-index facets disappear easily during NP formation because the rate of crystal growth in the direction perpendicular to a high-index facet with high surface energy is much faster than that along the normal direction of a low-index

[a]Institute of Theoretical Physics and Astrophysics, Department of Physics, Xiamen University, Xiamen 361005, China. E-mail: yhwen@xmu.edu.cn; Fax: +86-592-218-9426; Tel: +86-592-218-2248

[b]Center for Cloud Computing and Big Data, Department of Automation, Xiamen University, Xiamen 361005, China

[c]State Key Laboratory of Physical Chemistry of Solid Surfaces, Department of Chemistry, Xiamen University, Xiamen 361005, China

one. Therefore, it is extremely challenging to synthesize high-index-faceted NPs. Recently, significant progress has been made in the synthesis of tetrahexahedral (THH) Pt NPs bound with high-index facets such as {730}, {210} and {520} ones by an electrochemical route.[14,15] These THH Pt NPs exhibited greatly enhanced catalytic activity compared with the existing commercial Pt/C catalysts. Subsequently, THH Pd and Au NPs have also been prepared by the electrochemical and wet-chemical methods.[16,17] To further improve the chemical activity of metallic nanocatalysts, a feasible approach is to synthesize high-index-faceted bimetallic or multimetallic NPs by introducing other metallic elements selectively. A typical example is that the synthesized THH Pt–Pd alloy NPs, which are mainly enclosed by {10 3 0} high-index facets, exhibit catalytic activity at least three times higher than the THH Pd NPs, and six times higher than commercial Pd black catalysts for the electro-oxidation of formic acid due to the synergy effects of high-index facets and electronic structures of the alloy.[18] Furthermore, the THH NPs with entirely high-index {730} facets were found to display the best electrocatalytic activity in bimetallic Au–Pd NPs with tetrahexahedron, concave octahedron, and octahedron shape. Besides, the bimetallic (or multimetallic) NPs are crucial for exploiting the bifunctional (or multifunctional) catalytic activities.[19] A representative is bimetallic Pt–Au NPs in which Pt can provide a site for methanol oxidation reactions or oxygen reduction reactions and Au for adsorption of hydroxide groups or oxidation of CO to CO_2.[20,21]

Meanwhile, the thermodynamic stability of metallic NP catalysts is of considerable importance for their chemical synthesis and ultimate applications for the following two reasons: on one hand, the NPs tend to aggregate into larger particles due to the enhanced atomic diffusion when the ambient temperature reaches the Tammann temperature.[22] Thus, controlling the synthesis and catalytic temperature reasonably is of technological importance for preventing the sintering and coarsening of metallic NPs. On the other hand, most of the catalytic reactions take place on surfaces, and surface structures of NPs will thereby play key roles during the catalytic processes. Some of the catalytic reactions, such as the catalytic cracking of petroleum and the purification of automobile exhaust gases, are usually performed at high temperature. The high-index planes are more easily destroyed at elevated temperature owing to their higher surface energy compared with that of low-index ones such as {111} and {100}. Once the high-index-faceted surface structures are broken, the NPs will lose their excellent catalytic properties. Furthermore, composition distribution may be varied at different temperatures due to the differences of alloy elements in cohesive energy, surface energy, atomic radius and diffusivity. Hence, the examination on thermodynamic stability of metallic NPs is particularly helpful not only for suppressing their sintering and coarsening but also for stabilizing their high-index-faceted structures at high temperatures. Despite the continuously growing reports on the synthesis, characterization and catalytic performance of metallic NP catalysts with such open surface structures, however, there has not been an elaborate study on the thermodynamic stability of alloy NPs with different high-index facets.

In this article, the THH Pt–Pd alloy NPs bound with high-index facets were chosen to be investigated by atomistic simulations. Considering that the {730} surface is periodically composed of two {210} subfacets followed by one {310} subfacet, the {520} surface is periodically composed of one {210} subfacet followed by one {310} subfacet, and the {1030} surface is periodically composed of two {310} subfacets followed by one {410} subfacet, {210} and {310} surfaces can be regarded as representatives of high-index planes. Therefore, the THH Pt–Pd alloy NPs, enclosed with {210} and {310} high-index facets, have been examined in this work. Besides, the percentage of Pt atoms from 0 to 100% has been considered in modeling the THH Pt–Pd alloy NPs to trace the effects of Pt/Pd ratio. These NPs were continuously heated to examine their thermodynamic stabilities. Both the microstructure and shape at different temperatures were explored. To the best of our knowledge, this is the first report about the thermodynamic stability and shape evolution of polyhedral alloyed NPs with high-index facets. This article is structured as follows. Section 2 briefly describes the simulation methods. Section 3 presents the calculated results, discussion and comparison with available results. The main conclusions are summarized in the fourth section.

2. Simulation methodology

As is known, the THH NPs are bound by 24 facets of Miller indices {$hk0$} with at least one index being larger than unit.[14] The tetrahexahedron can be considered as a cube with each face capped by a square pyramid (see Fig. 1a). In order to reasonably accord with the experimentally observed structure and shape, THH Pt–Pd alloy NPs terminated by {210} and {310} facets were constructed from a large cubic fcc single crystal. Initially, Pt and Pd atoms are arbitrarily distributed in the NPs by computer-produced random seeds. As an example, Fig. 1b illustrates the cross-section structures of {310} faceted Pt–Pd alloy NPs with the Pt/Pd atomic ratio equal to one. To investigate the effects of Pt/Pd ratio on the stability, the Pt composition is continuously varied from 0 to 100% with an increment of 10%. Note that the Pt–Pd alloy NP will be evolved into the Pd monometallic one for the Pt percentage of zero and the Pt monometallic one for the Pt percentage of 100. To facilitate a comparison study, the side length of the cube was set at $12a_0$ in each tetrahexahedron (a_0 = 3.924 Å), corresponding to the particle size of 4.71 nm or so. Resultantly, the total number of atoms is 10 831 for {210} faceted NPs and 9553 for {310} faceted NPs.

In atomistic simulations, the quantum corrected Sutton–Chen (Q-SC) type potentials were adopted to describe the interatomic interactions.[23] These potentials represent many-body interactions, and their parameters are optimized to describe the lattice parameter, cohesive energy, bulk modulus, elastic constants, phonon dispersion, vacancy formation energy, and surface energy, leading to an accurate description of thermodynamic and transport properties of metals and their alloys.[24–27] The total potential energy for a system of atoms can be written as

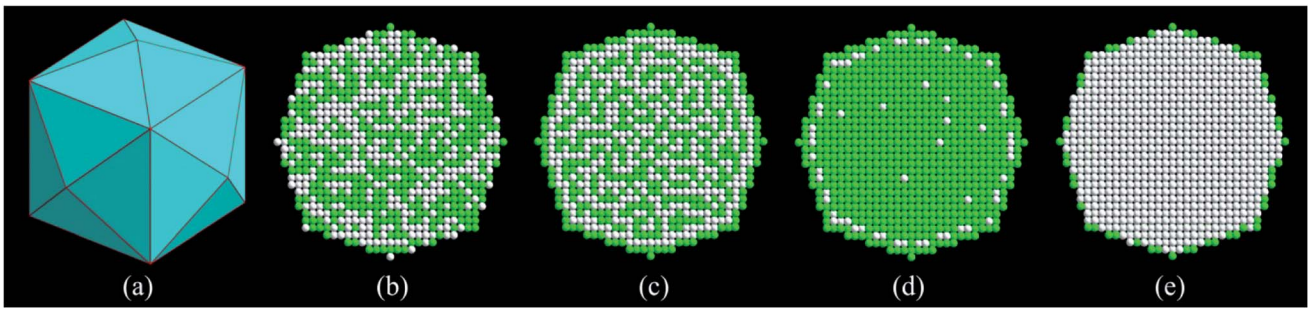

Fig. 1 Schematic illustration of THH Pt–Pd alloy NPs: (a) tetrahexahedral model, (b) initial configuration of {310} faceted NP with 50% Pt, energy minimization configurations of NPs with Pt compositions of (c) 50%, (d) 10%, and (e) 90%. Note that (b)–(e) present the cross-sections of NPs, and coloring denotes the type of atom: white, Pt atom; and bright green, Pd atom.

$$U = \sum_i U_i = \sum_i \varepsilon \left[\frac{1}{2} \sum_{j \neq i} V(R_{ij}) - c\sqrt{\rho_i} \right], \quad (1)$$

in which $V(R_{ij})$ is a pair interaction function defined by the following equation:

$$V(R_{ij}) = \left(\frac{a}{R_{ij}} \right)^n, \quad (2)$$

accounting for the repulsion between the i and j atomic cores; ρ_i is a local electron density accounting for cohesion associated with atom i defined as

$$\rho_i = \sum_{j \neq i} \left(\frac{a}{R_{ij}} \right)^m \quad (3)$$

In eqn (1)–(3), R_{ij} is the distance between atoms i and j; a is a length parameter scaling all spacings (leading to dimensionless V and ρ); c is a dimensionless parameter scaling the attractive terms; ε sets the overall energy scale; n and m are integer parameters such that $n > m$. Given the exponents (n, m), c is determined by the equilibrium lattice parameter, and ε is determined by the total cohesive energy.

The model parameters for Pt and Pd are listed in Table 1. In order to describe the atomic interaction between Pt and Pd, the geometric mean was used to obtain the energy parameter ε while the arithmetic mean was used for the remaining parameters.[28]

As the first stage of atomistic simulations, the energy minimization scheme should be applied to search the lowest-energy configurations of the modeled NPs. Note that the total energy at absolute zero could be obtained by summing the potential energy of each atom in the NPs. However, the prediction of energetically most stable structures is highly complicated for such large NPs because it is related to searching the minimum points on the potential energy surface, which corresponds to the stable states of the systems. In this article, the Monte Carlo (MC) method has been used for energy minimization due to its popularity and effectivity.[29] We have performed a series of Metropolis MC simulations in which both the number of total atoms and that of each element in the alloy NP are invariable, and the minimum-energy configurations of the systems at the ground state were predicted by optimizing their total energies with respect to their compositional exchange.[30] Considering that the predictive quality of MC simulations may be associated with the initial conditions, we have adopted different random seeds to produce various initial configurations. The MC simulations have been performed for at least 200 000 steps for the optimization of these configurations at absolute zero. To guarantee that the energy minimum is actually achieved at fixed tetrahexahedral shape and composition, we have also performed a series of MC simulated annealing. The annealing procedure was simulated from 1000 to 0 K at a cooling rate of 0.001 K per MC step. Fig. 1c–e illustrate the final configurations of THH Pt–Pd alloy NPs with Pt compositions of 50%, 10%, and 90%. These configurations show that the outermost layer is mainly composed of Pd atoms while the sub-outermost layer is preferentially occupied by Pt atoms, which is beneficial for minimizing the surface energy and total energy of Pt–Pd alloy NPs due to the surface energy of Pd being lower than that of Pt.[28]

Table 1 Potential parameters used in atomistic simulations of Pt–Pd alloy NPs

Element	n	m	ε (meV)	C	a (Å)
Pt	11	7	9.7894	71.336	3.9163
Pd	12	6	3.2864	148.205	3.8813

After initial energy minimization, molecular dynamics (MD) methods were employed to simulate the continuous heating process of all the NPs. To make the simulations more reliable, we employed constant volume and temperature molecular dynamics (*NVT*-MD) to allow energy fluctuations, which may be critical for the resulting dynamics. The NPs underwent the heating process consisting of a series of *NVT*-MD simulations from 0 to 1800 K with a temperature increment of 50 K. However, a smaller step of 10 K was adopted to investigate the melting behavior more accurately when the temperature reached to around the melting point. The simulations were carried out for 200 picoseconds of the relaxation time at each temperature, and the statistical quantities were obtained in the last 25 picoseconds. The desired temperature and ambient pressure were maintained by the Nose–Hoover thermostat[31] and Berendsen approach,[32] respectively. The equations of atomic motion were integrated by the velocity Verlet algorithm[33] with a femtosecond time step.

3. Results and discussion

Important information concerning the thermodynamic properties, the characteristics and progress of melting during the heating process can be obtained from data records from MD simulations. Experimentally, one effective way to study the phase transition is to investigate the caloric curve (energy *versus* temperature) of the system. To date, the caloric curves have been successfully used to detect the melting behavior of nanoparticles, nanowires, and bulk materials both experimentally and theoretically.[34,35] The heat capacity can be deduced from the caloric curve. Note that it has a sharp peak at some cases but it does not at others: the former cases have been called a first-order melting transition while the latter cases have often been called a second-order melting transition.[36] The melting temperature (T_m) is usually defined as a temperature at which the heat capacity reaches its maximum. We calculated the total potential energy as a function of temperature during the heating process and then deduced the heat capacity according to the following equation:[37]

$$C_p(T) = \frac{dU}{dT} + \frac{3}{2}R_{gc}, \quad (4)$$

where U is the potential energy, and $R_{gc} = 8.314$ J mol^{-1} K^{-1}.

As a representative, Fig. 2a shows the temperature dependence of potential energies and specific heat capacities of THH Pt–Pd alloy NPs with a Pt/Pd molar ratio of 1 : 1. For comparison, the results of THH Pt and Pd NPs are also presented in this figure. It can be observed from the figure that the gradual increase of potential energy is followed by a sudden upward jump, clearly indicating the occurrence of melting. The melting temperatures of pure Pt and Pd NPs are all remarkably lower than those of their bulk counterparts (2045 K for Pt and 1825 K for Pd, respectively).[38] This reduction should be attributed to the high surface–volume ratio in nano-sized particles and low surface premelting temperature associated with the weak bonds in the low-coordinated surface atoms, which have been verified by both experimental and theoretical studies.[34,35,39] Furthermore, the melting points of {210} faceted NPs are about 10 K higher than those of {310} faceted ones. By comparing with monometallic NPs, a notable feature is that the melting points of Pt–Pd alloy NPs are remarkably higher than those of pure Pd ones but lower than those of pure Pt NPs. Interestingly, two prominent peaks in the heat capacity curves of Pt–Pd core–shell NPs[40] have not been observed here. This difference reflects the strong dependence of the melting behaviors on the structures of bimetallic Pt–Pd NPs such as the detailed distribution of Pt and Pd atoms.

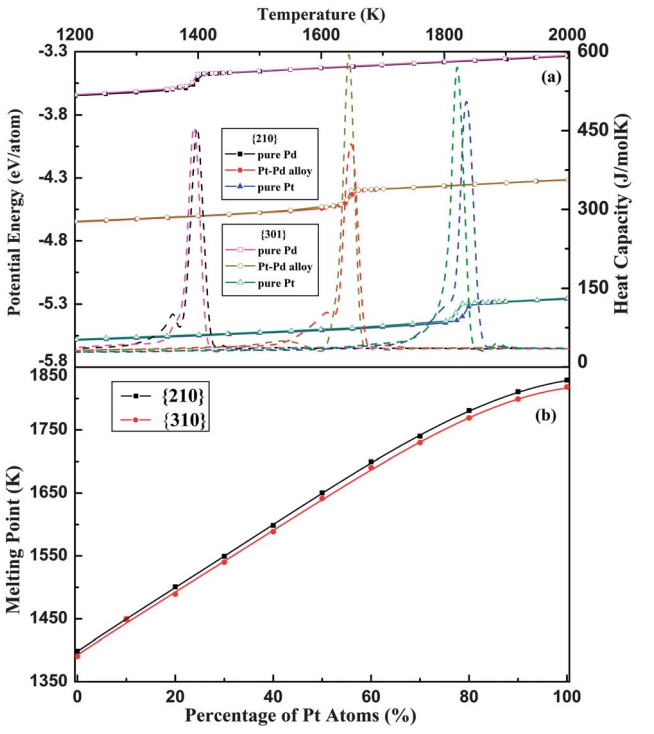

Fig. 2 (a) Temperature dependent potential energies and specific heat capacities of THH Pt NPs, Pd NPs, and Pt–Pd alloy NPs with 50% Pt composition. Note that the dashed lines correspond to the heat capacity. (b) Dependence of the melting points of Pt–Pd alloy NPs on the Pt composition.

Similarly, the melting temperatures of THH Pt–Pd alloy NPs with other Pt/Pd ratios can be identified from their caloric curves. Fig. 2b illustrates the melting point as a function of Pt composition. Evidently, the melting point of {210} faceted NPs is higher than that of {310} faceted ones at the same Pt/Pd ratio. With an average value of about 10 K, their differences are 8–12 K except for the NPs with 10% Pt composition. One should be careful when comparing their melting points because the possible error may lie in the MD simulations. For both faceted Pt–Pd alloy NPs, the melting point presents a close-linear increase with respect to the Pt composition below 60%, following a deviation from linearity for a high Pt composition. This progressive increase suggests that the addition of Pt element into Pd NPs can significantly enhance their melting points. The close-linear variation of melting points for alloy NPs can be attributed to the balance between the extent of surface melting and the radius of the remaining solid core.[41] At high Pt compositions, the surface melting will be reduced to a great extent, leading to nonlinear variation.

As is mentioned above, the melting points of alloy NPs are dependent not only on the surface structures of facets enclosing the particles but also on the Pt/Pd ratios. Therefore, it is necessary to further examine the melting behaviors of these NPs of different facets and compositions. Generally, the melting mechanism of materials can be detected through analysis of the structural evolution, diffusion coefficients, root-mean-square displacement of atoms and so on. However, the Lindemann index is a simple but effective measurement of thermally driven disorder. It is usually used to characterize the thermodynamic evolution of a system.[42] For a system of N atoms, the local Lindemann index for the i^{th} atom is defined as the root-mean-squared bond length fluctuation as[43]

$$\delta_i = \frac{1}{N-1}\sum_{j\neq i}\frac{\sqrt{\langle R_{ij}^2\rangle - \langle R_{ij}\rangle^2}}{\langle R_{ij}\rangle}, \quad (5)$$

and the system-averaged Lindemann index is calculated as

$$\bar{\delta} = \frac{1}{N}\sum_{i}\delta_i, \quad (6)$$

where R_{ij} is the distance between the i^{th} and j^{th} atoms. The Lindemann index was originally developed to study the melting behavior of bulk crystals. The Lindemann criterion suggests that the melting occurs when the index is in the range of 0.1–0.15, depending on materials, while a smaller critical index of about 0.03 was adopted in clusters and homopolymers due to the relaxed constraint of the surface atoms.[44]

The temperature dependent Lindemann indices during the heating process were respectively calculated for Pt and Pd atoms in both faceted Pt–Pd alloy NPs (not shown here). By investigating the Lindemann index curves of pure Pt and Pd NPs, we found that the critical value of Lindemann index should be ascertained to be 0.039 and 0.044 for Pt and Pd atoms, respectively. This suggests that different critical values should be adopted when one use the Lindemann criterion to investigate the melting behavior of bimetallic particles. In order to visualize the melting process at the atomic level, we have extracted some snapshots of all the NPs taken at representative temperatures during the simulation of continuous heating. As a representative, Fig. 3 illustrates the snapshots of {310} faceted alloy NPs with 50% Pt composition at six temperatures. In these snapshots, the concept of Lindemann atom was introduced:[45] the atom whose Lindemann index exceeds the critical value (0.039 for Pt and 0.044 for Pd) is defined as the Lindemann atom; otherwise it is noted as the non-Lindemann atom.

As shown in Fig. 3a, the Pt–Pd alloy NP retains a clear-cut fcc arrangement at a room temperature of 300 K. No change is found in both the surface structure and shape compared with its initial configuration. With the temperature increased to 450 K, atoms at eight corner sites firstly move inward, while those at six apices remained at their initial positions. The common neighbor analysis (CNA)[46] shows that the former are three-coordinated, and the latter are four-coordinated. This indicates that the less-coordinated atoms diffuse away more easily as the temperature is increased. The apex atoms are stable until 900 K. Further heating will push them to leave their initial positions and to diffuse towards the steps in facets. Meanwhile, some atoms on the edges also start to deviate from their original positions. Nevertheless, the NP preserves the tetrahexahedral shape well at 1000 K, and {310} facets can be discernible (see Fig. 3b). By comparing Fig. 3a and b, it is ascertainable that no significant diffusion can be observed for the interior atoms, unlike the surface ones.

As is known, the atomic diffusion activities highly depend on the ambient temperature. Due to the low coordination number, surface atoms exhibit higher mobility than the interior ones so that surface diffusion is faster than bulk diffusion. The snapshot of the NP at 1300 K indicates that all corner atoms disappear, and the edges become obtuse although the atomic steps are still resident on the surface (see Fig. 3c). With the temperature increased up to 1600 K, the {310} facets have absolutely been destroyed, and the NP has already lost the tetrahexahedral shape. Moreover, the premelting has been initiated on the surface, as shown in Fig. 3d. Once the melting extends over the entire surface, it will spread into the interior region progressively. At this time, the NP can be regarded as a mixture consisting of a liquid shell and a solid core (see Fig. 3e). This morphology is chemically interesting because the liquid metal atoms on the surface of solid particles could facilitate the dissolution of adsorbates due to their enhanced mobility,

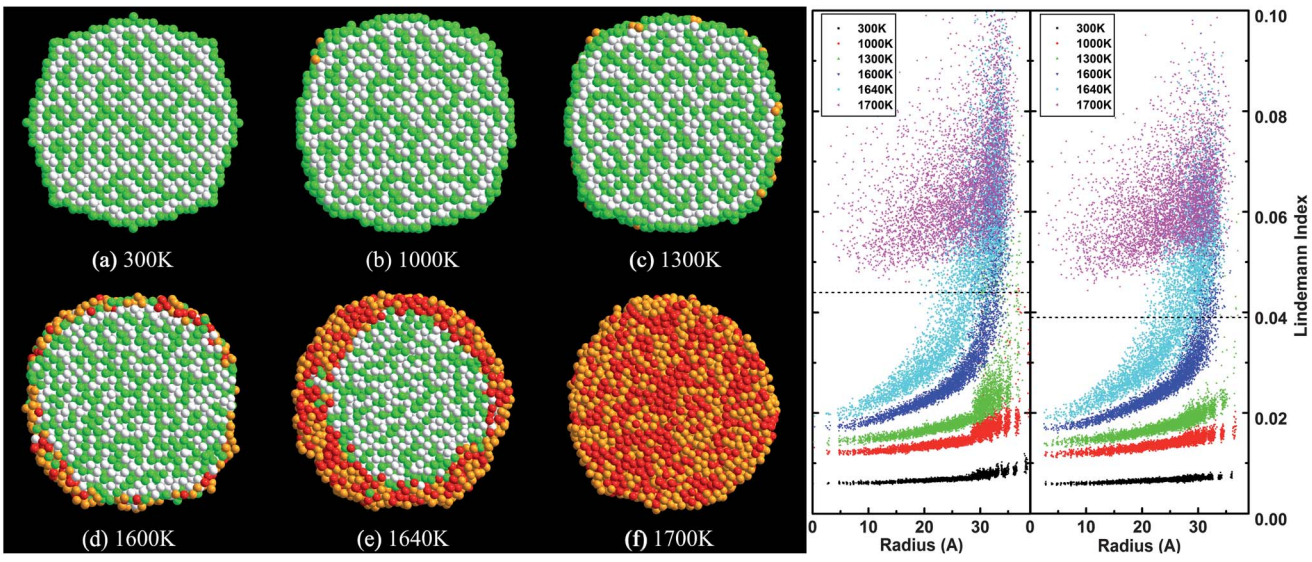

Fig. 3 (a)–(f) present the snapshots of cross-sections of {310} faceted Pt–Pd alloy NPs with 50% Pt composition taken at six representative temperatures. Coloring denotes the type of atom: white, Pt non-Lindemann atom; green, Pd non-Lindemann atom; red, Pt Lindemann atom; and orange, Pd Lindemann atom. (g) and (h) respectively illustrates the Lindemann index distributions of Pt and Pd atoms at the temperatures corresponding to (a)–(f). Note that the horizontal axis denotes the distance between the atom and particle center of mass, and the dashed line indicates the critical Lindemann index: 0.044 for Pd in (g) and 0.039 for Pt in (h).

enabling the occurrence of different chemical processes.[47] At 1700 K, a typical liquid NP can be clearly seen from the atomistic image illustrated in Fig. 3f. The outer shell is dominated by Pd atoms while Pt atoms are preferentially distributed in the inner core. This aggregation behavior is driven by the fact that Pd has significantly lower surface energy than Pt.[48]

Fig. 3g and h show the Lindemann index distributions of Pt and Pd atoms in the THH NP at different temperatures, respectively. Evidently, the Lindemann index of atoms increases with temperature, and the atoms in the outer layer possess higher Lindemann indices than those in the inner layer. This should be associated with their different abilities of atomic diffusion. In fact, both the Lindemann index and diffusion coefficient can be characterized by the atomic mean-square displacement, which is directly related to the ambient temperature and atomic position. By comparing the two figures, it can be found that Pd atom has a higher Lindemann index than Pt atom at the same layer and temperature, which is attributed to the lower atomic radius and smaller atomic mass of Pd compared with Pt.[49] Besides, it is directly seen from these figures that the melting starts on the surface and gradually propagates into the core, consistent with previous studies.[25–28] It is worth noting that these results, as mentioned above, still keep valid for {310} faceted NPs with other Pt/Pd ratios and {210} faceted NPs after carefully checking their thermodynamic evolution during the heating process.

It is well-known that the catalytic reactions preferentially take place on the surface. Therefore, surface characteristics have an important effect on the catalytic activity, and play a crucial role at some stages of chemical processing. From the aforementioned results, it is observed that the high-index-faceted surface of THH NPs is changed with increasing temperature, and is finally evolved into the sphere-like surface before the overall melting. Once the initial surface structures are broken, the THH NPs will lose their excellent catalytic properties. Hence, it is essential to ascertain the critical temperature of surface transformation, which could help optimize the synthesis and the catalytic operating temperatures. However, it is rather difficult to accurately detect the surface changes due to small facets in nano-sized particles. Considering that the Miller index of facets determines the shapes of polyhedra, the shape change is indicative of the surface transformation of NPs. To precisely characterize the shape, here we introduce the shape factor S as follows:[50]

$$S = \frac{1}{R^2}\sqrt{\frac{1}{N}\sum_{i=1}^{N}\left(r_i^2 - R^2\right)^2}, \quad (7)$$

in which r_i is the distance of atom i from the particle center of mass and R is the root-mean-square of r_i:

$$R = \sqrt{\frac{1}{N}\sum_{i=1}^{N} r_i^2}. \quad (8)$$

According to this definition, the shape factors of monometallic THH NPs with an ideal fcc lattice structure are about 0.451 and 0.465 for {210} and {310} facets, respectively, independent of the total number of atoms in the NPs. Actually, the value of shape factor is slightly deviated from the ideal one due to the surface relaxation of NPs. For bimetallic or multimetallic NPs, it is also affected by the atomic radius ratio and molar ratio of alloy elements.

Fig. 4 demonstrates the temperature dependent shape factors of {210} and {310} faceted Pt–Pd alloy NPs during the heating process. Due to the similar tetrahexahedral shape for all the Pt/Pd atomic ratios, the shape factors basically keep at around 0.452 for {210} facets and 0.467 for {310} facets. They fluctuate slightly around the mean values (see the dashed lines in Fig. 4) at low temperatures (typically below 750 K), which should be associated with the thermal motions of atoms at non-zero temperatures. However, as the temperature is further elevated, all the shape factors present a continuous decrease. Once the NPs have completely melted, they would experience larger fluctuation.

From Fig. 4, there are two main results worth noting. One is that the critical temperature at which the shape factor begins to continuously decrease is dependent on the Pt composition although its initial value is independent of the Pt/Pd ratio. In both faceted NPs, the critical temperature is increased with increasing Pt ratio, indicating that the addition of Pt can solidify the shapes of Pt–Pd alloy NPs. Also, this implies that the NP with higher Pt ratio possesses better shape stability, in agreement with the results of the thermodynamic stability aforementioned. Another result is that the critical temperature of shape factor is remarkably lower than the melting point. This means that the shapes of THH NPs have significantly changed prior to their overall melting, as indicated by Fig. 3.

The above analyses show that the {210} faceted NPs present higher critical temperature of melting and shape transformation, indicating their better thermodynamic and shape stabilities compared with the {310} faceted NPs. Although the surface energy of {210} planes is higher than that of {310} ones for fcc metals,[51] the surface energy seems not to be the determinant of particle stability. By comparison, arrangements of

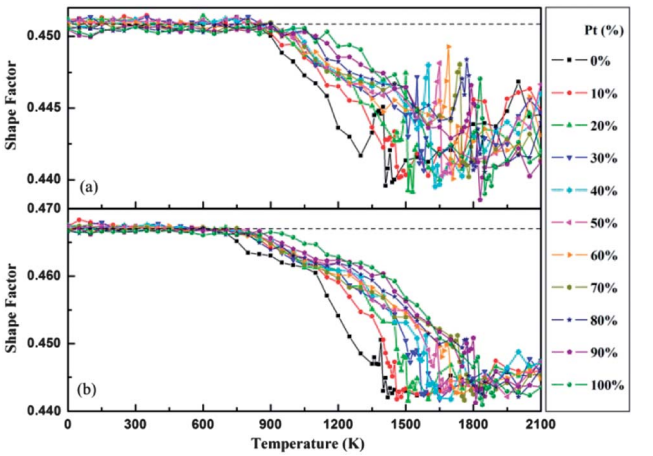

Fig. 4 Shape factors of (a) {210} and (b) {310} faceted THH NPs as a function of temperature. Dashed lines indicate the initial values at low temperatures.

surface atoms, which are commonly determined by the surface Miller index and directly reflect the atomic distribution of apices, edges, steps and facets, could play more important roles in determining the thermodynamic and shape stabilities of NPs because their instability generally starts from surface destruction. These surface atoms have different coordination numbers, depending on their local environments. They are generally low-coordinated (less than 12 for fcc metals), and usually act as catalytic active sites. Precisely due to the low atomic coordination, they move away from their initial positions more easily than bulk atoms under thermal driving forces at elevated temperatures. Therefore, we use the concept of coordination number to analyze the arrangement characteristics of surface atoms in the THH NPs. Here, the low-coordinated atoms are defined as surface atoms. Fig. 5 shows the coordination number distribution of atoms in the {210} and {310} faceted NPs. Evidently, it is observed that the coordination numbers of atoms occupying the apices and edges in the {210} faceted NPs are similar to those in the {310} faceted ones. The atomic coordination number is three and four for eight cubic and six pyramidal apices, respectively. As seen in Fig. 3, these apex atoms first move away from their initial geometrical positions when subjected to heating. Those atoms occupying the eight cubic and twenty-four pyramidal sides (see the model in Fig. 1a) have five-fold coordination, therefore these sides are destroyed following the apices. The differences between the {210} and {310} facets lie in the steps: each step has two rows of atoms in the former while three rows in the latter (see Fig. 5a and b). Although the atoms in the outer and inner rows respectively have six- and nine-fold coordination for both the {210} and {310} facets, the atoms in the middle row of the {310} facets are eight-coordinated. These eight-coordinated atoms can initiate their thermally driven migrations at lower temperature than the nine-coordinated ones. Therefore, it is expectable that the {310} facets are more easily destroyed than the {210} ones at elevated temperatures. Also, through the analyses of coordination number distribution, we find that the average coordination number of surface atoms is 8.38 for the {210} faceted NPs and 8.17 for the {310} faceted NPs. The high coordination number is beneficial for stabilizing the atomic arrangement at the surface, thus the {210} faceted NPs should exhibit better thermodynamic and shape stabilities compared with the {310} faceted NPs.

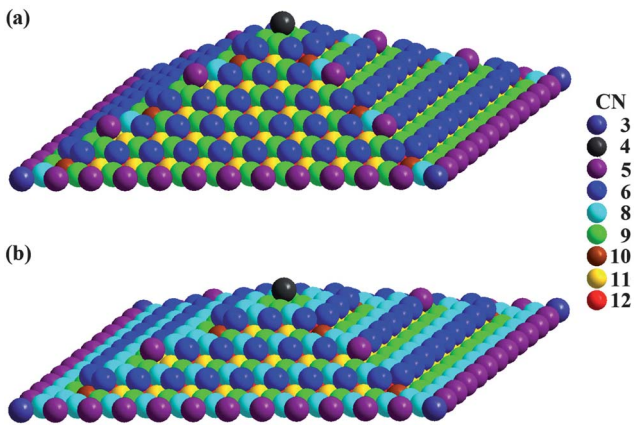

Fig. 5 Coordination number (CN) of atoms in one of the six square pyramids for (a) {210} and (b) {310} faceted NPs.

4. Conclusions

In summary, we have employed atomistic simulations to systematically investigate the thermodynamic stability of THH Pt–Pd alloy NPs enclosed by {210} and {310} facets. The Lindemann index, shape factor, and coordination number were adopted to characterize the melting behavior and thermodynamic evolution of NPs. The Monte Carlo energy minimization procedure indicated that the outermost layer is mainly composed of Pd atoms while the sub-outermost layer is preferentially occupied by Pt atoms in the NPs. Our simulations have revealed that the thermodynamic stability of Pt–Pd NPs is strongly dependent on the surface structures of facets enclosing the particles and the Pt/Pd ratios: the THH NPs enclosed by {210} facets exhibit better thermodynamic stability than those bound by {310} facets at the same side length and Pt/Pd ratio. The former have about 10 K higher melting point than the latter. Meanwhile, a high Pt composition will help enhance their melting temperature. The atomistic snapshots have demonstrated that for both faceted THH NPs, the melting process starts on the surface and gradually propagates into the core region, in agreement with previous studies. The analyses of shape factor show that shape changes occur prior to the overall melting, and {210} faceted NPs have better shape stability than {310} faceted ones. The atomic coordination number has been used to elucidate the potential origin of the different stabilities. These results suggest that the thermodynamic and shape stabilities of THH alloy NPs could be tunable by adjusting the surface Miller index and the molar ratio of alloy elements, indicating a highly promising strategy to synthesize high-index-faceted NPs of high catalytic performance and excellent stability. Also, our study indicates that it is possible to tailor the distribution of atoms in bimetallic or multimetallic NPs by controlling the alloy composition and annealing temperature, which is desirable for improving the selectivity of catalysts for chemical reactions. This study is expected to have important implications not only in the exploitation of high-index-faceted bimetallic NPs, but also in the further design of multimetallic NP catalysts.

Acknowledgements

This work is supported by the National Natural Science Foundation of China (Grant no. 21021002, 51271156, and 11204252), the Natural Science Foundation of Fujian Province of China (Grant no. 2013J06002), and the Fundamental Research Funds for the Central Universities of China (Grant no. 2012121010).

Notes and references

1 R. W. Murray, *Chem. Rev.*, 2008, **108**, 2688–2720.
2 Z. Y. Zhou, N. Tian, J. T. Li, I. Broadwell and S. G. Sun, *Chem. Soc. Rev.*, 2011, **40**, 4167–4185.

3 P. K. Jain, I. H. El-Sayed and M. A. El-Sayed, *Nano Today*, 2007, **2**, 18–29.
4 T. K. Sau, A. L. Rogach, F. Jackel, T. A. Klar and J. Feldmann, *Adv. Mater.*, 2010, **22**, 1805–1825.
5 C. Noguez, *J. Phys. Chem. C*, 2007, **111**, 3806–3819.
6 Z. L. Wang, *J. Phys. Chem. B*, 2000, **104**, 1153–1175.
7 K. M. Bratlie, H. Lee, K. Komvopoulos, P. Yang and G. A. Somorjai, *Nano Lett.*, 2007, **7**, 3097–3101.
8 T. S. Ahmadi, Z. L. Wang, T. G. Green, A. Henglein and M. A. El-Sayed, *Science*, 1996, **272**, 1924–1926.
9 H. Lee, S. E. Habas, S. Kweskin, D. Butcher, G. A. Somorjai and P. D. Yang, *Angew. Chem., Int. Ed.*, 2006, **45**, 7824–7828.
10 J. Ren and R. D. Tilley, *J. Am. Chem. Soc.*, 2007, **129**, 3287–3291.
11 Y. G. Sun and Y. N. Xia, *Science*, 2002, **298**, 2176–2179.
12 S. Y. Zhao, S. H. Chen, S. Y. Wang, D. G. Li and H. Y. Ma, *Langmuir*, 2002, **18**, 3315–3318.
13 N. Tian, Z. Y. Zhou and S. G. Sun, *J. Phys. Chem. C*, 2008, **112**, 19801–19817.
14 N. Tian, Z. Y. Zhou, S. G. Sun, Y. Ding and Z. L. Wang, *Science*, 2007, **316**, 732–735.
15 Z. Y. Zhou, Z. Z. Huang, D. J. Chen, Q. Wang, N. Tian and S. G. Sun, *Angew. Chem., Int. Ed.*, 2010, **49**, 411–414.
16 N. Tian, Z. Y. Zhou, N. F. Yu, L. Y. Wang and S. G. Sun, *J. Am. Chem. Soc.*, 2010, **132**, 7580–7581.
17 T. Ming, W. Feng, Q. Tang, F. Wang, L. D. Sun, J. F. Wang and C. H. Yan, *J. Am. Chem. Soc.*, 2009, **131**, 16350–16351.
18 Y. J. Deng, N. Tian, Z. Y. Zhou, R. Huang, Z. L. Liu, J. Xiao and S. G. Sun, *Chem. Sci.*, 2012, **3**, 1157–1161.
19 C. L. Lu, K. S. Prasad, H. L. Wu, J. A. Ho and M. H. Huang, *J. Am. Chem. Soc.*, 2010, **132**, 14546–14553.
20 P. H. Fernndez, S. Rojas, P. Ocon, J. L. G. Fuente, J. S. Fabian, J. Sanza, M. A. Pena, F. J. G. Garcia, P. Terreros and J. L. G. Fierro, *J. Phys. Chem. C*, 2007, **111**, 2913–2923.
21 J. Zhang, K. Sasaki, E. Sutter and R. R. Adzic, *Science*, 2007, **315**, 220–222.
22 J. M. Sun, D. Ma, H. Zhang, X. M. Liu, X. W. Han, X. H. Bao, G. Weinberg, N. Pfander and D. S. Su, *J. Am. Chem. Soc.*, 2006, **128**, 15756–15764.
23 T. Cagin, Y. Kimura, Y. Qi, H. Li, H. Ikeda, W. L. Johnson and W. A. Goddard, *Mater. Res. Soc. Symp. Proc.*, 1999, **554**, 43–48.
24 Y. H. Wen, Y. Zhang, J. C. Zheng, Z. Z. Zhu and S. G. Sun, *J. Phys. Chem. C*, 2009, **113**, 20611–20617.
25 R. Huang, Y. H. Wen, Z. Z. Zhu and S. G. Sun, *J. Mater. Chem.*, 2011, **21**, 11578–11584.
26 R. Huang, Y. H. Wen, Z. Z. Zhu and S. G. Sun, *J. Phys. Chem. C*, 2012, **116**, 8664–8671.
27 Y. H. Wen, R. Huang, C. Li, Z. Z. Zhu and S. G. Sun, *J. Mater. Chem.*, 2012, **22**, 7380–7386.
28 S. K. R. S. Sankaranarayanan, V. R. Bhethanabotla and B. Joseph, *Phys. Rev. B: Condens. Matter Mater. Phys.*, 2005, **71**, 195415.
29 A. R. Leach, *Molecular Modelling: Principles and Applications*, Pearson Education Ltd., London, 2001.
30 K. Yun, Y. H. Cho, P. R. Cha, J. Lee, H. S. Nam, J. S. Oh, J. H. Choi and S. C. Lee, *Acta Mater.*, 2012, **60**, 4908–4916.
31 D. L. Evans and B. L. Holian, *J. Chem. Phys.*, 1985, **83**, 4069–4074.
32 H. J. C. Berendsen, J. P. M. Postma, W. F. van Gunsteren, A. DiNola and J. R. Haak, *J. Chem. Phys.*, 1984, **81**, 3684–3690.
33 W. C. Swope, H. C. Anderson, P. H. Berens and K. R. Wilson, *J. Chem. Phys.*, 1982, **76**, 637–649.
34 G. A. Breaux, C. M. Neal, B. Cao and M. F. Jarrold, *Phys. Rev. Lett.*, 2005, **94**, 173401.
35 J. Kang, S. H. Wei and Y. H. Kim, *J. Am. Chem. Soc.*, 2010, **132**, 18287–18291.
36 Z. H. Li and D. G. Truhlar, *J. Am. Chem. Soc.*, 2008, **130**, 12698–12711.
37 Y. Qi, T. Cagin, W. L. Johnson and W. A. Goddard, *J. Chem. Phys.*, 2001, **115**, 385–394.
38 C. Kittel, *Introduction to Solid State Physics*, John Wiley & Sons, New York, 1996.
39 Q. S. Mei and K. Lu, *Prog. Mater. Sci.*, 2007, **52**, 1175–1262.
40 R. Huang, Y. H. Wen, Z. Z. Zhu and S. G. Sun, *J. Phys. Chem. C*, 2012, **116**, 11837–11841.
41 S. K. R. S. Sankaranarayanan, V. R. Bhethanabotla and B. Joseph, *Phys. Rev. B: Condens. Matter Mater. Phys.*, 2005, **72**, 195405.
42 H. Lowen, *Phys. Rep.*, 1994, **237**, 249–324.
43 Y. Shibuta and T. Suzuki, *Chem. Phys. Lett.*, 2007, **445**, 265–270.
44 Y. Q. Zhou, M. Karplus, K. D. Ball and R. S. Berry, *J. Chem. Phys.*, 2002, **116**, 2323–2329.
45 Z. H. Jin, P. Gumbsch, K. Lu and E. Ma, *Phys. Rev. Lett.*, 2001, **87**, 055703.
46 J. D. Honeycutt and H. C. Andersen, *J. Phys. Chem.*, 1987, **91**, 4950–4963.
47 B. Cao, A. K. Starace, O. H. Judd and M. F. Jarrold, *J. Am. Chem. Soc.*, 2009, **131**, 2446–2447.
48 L. Z. Mezey and J. Giber, *Surf. Sci.*, 1982, **117**, 220–231.
49 B. H. Morrow and A. Striolo, *Phys. Rev. B: Condens. Matter Mater. Phys.*, 2010, **81**, 155437.
50 Z. L. Wang, Z. Q. Zhong and S. Y. Wang, *Text. Res. J.*, 2012, **82**, 454–462.
51 Y. N. Wen and H. M. Zhang, *Solid State Commun.*, 2007, **144**, 163–167.

